LINEAR DYNAMICS OF THE FLOW-STRUCTURE INTERACTION OF COMPLIANT WALLS HAVING COMPLEX BOUNDARY CONDITIONS

M.W. Pitman & A.D. Lucey
Fluid Dynamics Research Group, Curtin University of Technology, Perth, Australia

ABSTRACT

A method for extracting the eigenvalues and eigenmodes from complex coupled fluid-structure interaction (FSI) systems is presented. The FSI system considered in this paper comprises a one-sided incompressible potential flow over a finite-length compliant wall. The flow field is determined by constructing a boundary-element solution of the Laplace equation, while finite-differences are used to solve a modified beam equation for the compliant-wall motion. The crux of the method lies in reducing the system equations to a single set of coupled linear differential equations in the interface variable. Thereafter, standard Krylov subspace projection methods are used to extract the system eigenvalues. The method is used to investigate the effect on stability of modifications to the well-studied case of a simple elastic plate held at both its ends. Of particular note in our results is that the addition of a restraint on the panel can trigger single-mode flutter at pre-divergence-onset flow speeds. We explain the existence of this new instability in terms of the changed phase-relation between wall motion and the fluid loading caused by added restraint.

1. INTRODUCTION

This paper revisits what is perhaps the most fundamental problem in flow-structure interaction, that of a potential flow interacting with a flexible panel that surmounts a baffle. The panel-flutter problem has a long history of investigation that stems from the work of Dugundji et al (1963) who first showed that with increasing applied flow speed, the panel succumbs first to divergence (or bucking) instability that gives way to modal-coalescence flutter at higher flow speeds. This problem continues to receive attention because its apparent simplicity masks some extraordinarily complex dynamics as evidenced by, for example, [2-4]. Pitman and Lucey (2007) have re-addressed the original problem using a new approach that can extract the exact eigenmodes of the system in a rational limit of discretisation.

In this paper we apply that method to the study of panels with complex boundary conditions, related to the configurations of Peake (2004), and to panels with spatially varying properties. By doing so, we show how the introduction of additional constraints can create a new type of instability within the system.

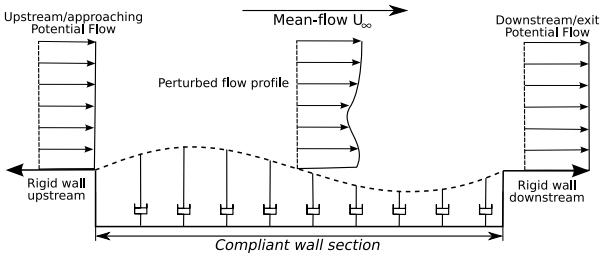

Figure 1: Schematic of the FSI system studied; the spring and dashpot foundations are absent for an unsupported elastic plate.

A schematic of the fluid-structure system modelled is shown in Fig. 1. It comprises a finite-length flexible flat plate held at both its ends; to investigate more complex types of complaint wall we can include a uniformly distributed spring foundation and dashpot-type damping, the latter to mimic the effect of energy dissipation in the plate/wall material. The plate/wall interfaces a uniform flow, the perturbations to which are assumed irrotational. We therefore neglect viscous effects and thus the model is an approximation to (infinitely) high-Reynolds number flow and cases where the boundary layer is very thin relative to disturbance wavelength.

2. SYSTEM EQUATIONS

In this paper the linear motion of the compliant wall is governed by the two-dimensional beam equation with an extra term added to account for the addition of a uniform dashpot-type damping ($d\partial\eta/\partial t$) to model the effects of energy dissipa-

tion in the structure.

$$\rho_m h \frac{\partial^2 \eta}{\partial t^2} + d\frac{\partial \eta}{\partial t} + B\frac{\partial^4 \eta}{\partial x^4} = -\Delta p(x,0,t) \quad , \quad (1)$$

where $\eta(x,t)$, ρ_m, h and B are, respectively, the plate's deflection, density, thickness and flexural rigidity, while $p(x,y,t)$ is the unsteady fluid pressure. In the present problem we apply hinged-edge conditions at the leading and trailing edges of the plate although in the method that follows there is no necessary restriction on such boundary conditions.

The fluid is modelled using the assumptions of incompressible and irrotational flow. This is an appropriate approximation for the high Reynolds number flow outside the boundary layer. However, rotationality and viscous effects of the boundary layer are ignored. This therefore implies the boundary layer is thin with respect to the wall disturbance wavelength and amplitude. A velocity perturbation potential $\phi(x,y,t)$, satisfying Laplace's equation and subject to the interfacial kinematic condition, is introduced, the solution of which is then used in the linearised unsteady Bernoulli equation,

$$\Delta p = -\rho\frac{\partial \phi}{\partial t} - \rho U_\infty \frac{\partial \phi}{\partial x} \quad , \quad (2)$$

where ρ and U_∞ are, respectively, the fluid density and flow speed.

3. EIGENVALUE DETERMINATION

Where Lucey and Carpenter (1992) used an explicit time-marching scheme for the solution of the wall position, the objective here is to avoid temporal discretisation by direct solution of a single set of ordinary differential equations. The deflection of the fluid-structure interface $\eta(x,t)$ will be the single resulting variable.

A boundary-element solution for the flow field is expressed as the sum of a mean flow plus a distribution of singularities along the deforming interface. In this case, zero-order linear source(-sink) elements are chosen for the singularities, with the strength of each element denoted $\sigma(x)$. With the discretisation of the compliant surface into N elements, each with constant strength σ_i, the vector of element strengths may be determined through a balance of the normal velocity components at the wall

$$\{\sigma\} = 2U_\infty[D_1]\{\eta\} + 2\{\dot{\eta}\} \quad , \quad (3)$$

where $\{\eta\}$ is the vector of interfacial displacements at the N evaluation points, the overdot denotes time-differentiation, and $[D_1]$ is the first-order spatial differentiation finite-difference matrix operator.

The singularity strengths (σ) determined through Eqn. 3 are used to evaluate the tangential velocity and perturbation potential for each element of the interface. Substitution of these expressions and Eqn. 3 into Eqn. 2, yields an expression for the forcing pressure in terms of the interfacial displacement alone giving

$$\begin{aligned} -\{\Delta p\} =& 2\rho U_\infty^2[T][D_1]\{\eta\} + 2\rho U_\infty[T]\{\dot{\eta}\} \\ &+2\rho U_\infty[T][\Phi]\{\dot{\eta}\} + 2\rho[\Phi]\{\ddot{\eta}\} \quad , \end{aligned} \quad (4)$$

where $[T]$ is the matrix of tangential-velocity influence coefficients. The form of Eqn. 4 shows the pressure to comprise the hydrodynamic stiffness (curvature effects), followed by two terms that yield the hydrodynamic damping (Coriolis' effects) and the final term that represents the hydrodynamic inertia (added-mass effects). The solution method for the flow field is described in more detail in Lucey et al (1997) wherein expressions for the various influence coefficients are listed.

The wall equation, Eqn. 1, is couched in finite-difference form using a set of N lumped-mass points that correspond to the boundary-element panel control points. Substituting the pressure-perturbation vector of Eqn. 4 into this finite difference expression gives

$$\{\ddot{\eta}\} = [E]\{\dot{\eta}\} + [F]\{\eta\} \quad , \quad (5)$$

where

$$\begin{aligned} [E] =& (\rho_m h[I] - 2\rho[\Phi])^{-1} \times \\ & (2\rho U_\infty[T] + 2\rho U_\infty[T][\Phi] - d[I]) \quad , \\ [F] =& (\rho_m h[I] + 2\rho[\Phi])^{-1} \times \\ & \left(2\rho U_\infty^2[T][D_1] - B[D_4][\Phi] - K[I]\right) \quad . \end{aligned}$$

where $[I]$ is the identity matrix and $[D_4]$ is the fourth-order spatial differentiation (penta-diagonal) matrix operator.

We now solve Eqn. 5 using a standard state-space method. The second-order $N \times N$ system is transformed to the following first-order $2N \times 2N$ system

$$\{\dot{w}\} = [H]\{w\} \quad , \quad (6)$$

where

$$[H]\{w\} = \begin{bmatrix} 0 & I \\ -F & E \end{bmatrix} \begin{Bmatrix} \{\eta\} \\ \{\dot{\eta}\} \end{Bmatrix} \quad , \quad (7)$$

for the new variable w. Assuming that all parts of the system move with the complex frequency, $s = s_R + \mathrm{i}s_I$, we can write

$$w = W \exp(st) \quad , \tag{8}$$

and substituting this into Eqn. 6, yields

$$(s[I] - [H])\{W\} = 0 \quad . \tag{9}$$

The solution of $\det(s[I] - [H]) = 0$ then generates the eigenvalues. These have been evaluated using the ARPACK solver through the EIGS command in the MATLAB software. Having found the eigenvalues, these can then be substituted back into Eqn. 9 to extract the complex eigenmode, $\{W\}^T$ for the N interfacial points.

4. RESULTS

In the results presented in this section, we use the non-dimensional scheme of Lucey et al (1997). This scheme is appropriate for the finite system studied here. The non-dimensional control parameter (stiffness ratio) and time are given by

$$\Lambda^F = \frac{\rho U_\infty^2 L^3}{B}, \; t' = \left\{ \frac{\sqrt{B/\rho_m h}}{L} \right\} \left(\frac{1}{h} \right) t. \tag{10a,b}$$

Additionally, for cases where structural damping is introduced, the non-dimensional damping coefficient is,

$$d' = \left(\frac{L^2}{2\pi^2 \sqrt{\rho_m (B}} \right) d \quad . \tag{11}$$

4.1. Simple elastic plate

Figure 2 shows the variation of eigenvalues with non-dimensional stiffness ratio. The stiffness ratio Λ^F could be interpreted as a measure of the flow speed for given plate properties. Figs. 2a and 2b are the variation of the non-dimensional oscillatory, s'_I, and growth/decay, s'_R, parts of the eigenvalues respectively. The solution can be broken into four regions, these being: a neutrally stable pre-divergence region, a divergence loop, a small neutrally stable divergence recovery zone, and finally a region of modal coalescence flutter. Figures 2c, 2d and 2e show snapshots of the wall motion for modes in the pre-divergence, divergence and divergence-recovery zones respectively. In these, and following modal plots, the thick line indicates the final wall position in the time-sequence of plots; the wall-position snapshots are the eigenmodes that correspond to the eigenvalues at specific points in the associated eigenvalue plots.

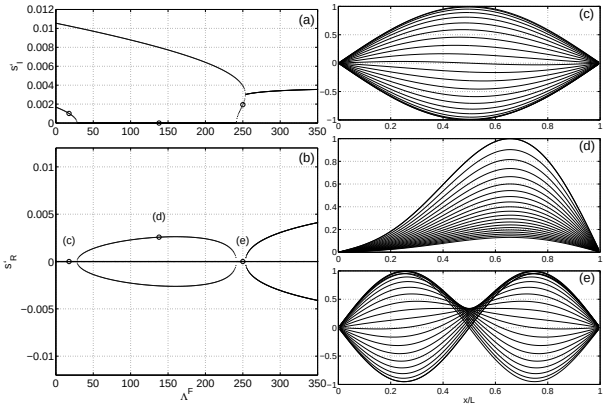

Figure 2: Elastic-plate. Eigenvalues and snapshots of wall motion at various flow speeds, Mode-1 amplifying, for $t' : 0 \rightarrow 793$ over 20 time steps each of duration $\Delta t' = 39.6$ at: (c) $\Lambda^F = 17.6$, (d) $\Lambda^F = 138$, and (e) $\Lambda^F = 250$.

4.2. Inhomogeneous flexible plates

Figure 3 shows the variation of eigenvalues and eigenmode snapshots for a wall with identical properties as the simple elastic plate used in Fig. 2, except that the flexural rigidity parameter of the wall (B) is varied linearly along the length of the wall. In this case, the mean value of the flexural rigidity (B_{AV}) is identical to the uniform value of Fig. 2 and the non-dimensional stiffness ratio Λ^F is based on this value. The gradient is set so that B varies from $1.95B_{AV}$ at the upstream edge down to $0.05B_{AV}$ at the trailing edge.

Figures 3c, 3d and 3e show snapshots of the unstable eigenmodes at various stages throughout the divergence loop. Qualitatively, the form of both the eigenvalue and eigenmode plots of Fig. 3 are similar to Fig. 2. However, the addition of a linear variation of the flexural rigidity such that the upstream end is more rigid than the downstream end tends to push the divergence loop down and to the right. This indicates that stiffening the upstream half of an elastic plate tends to stabilise the system in a similar manner to the addition of structural damping. Conversely, computations performed with a stiffened downstream end tended to destabilise the system by pushing the divergence loop up and to the left.

4.3. Multiple hinged boundary conditions

Figure 4 shows results for the same elastic plate as that used for Fig. 2, except that an extra hinge constraint has been added at a distance of

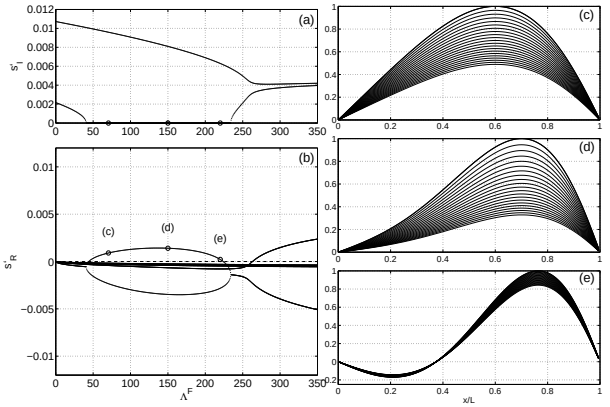

Figure 3: Elastic plate with material inhomogeneity. Eigenvalues and snapshots of wall motion in the divergence range of flow speeds, Mode-1 amplifying, for $t' : 0 \rightarrow 793$ over 20 time steps each of duration $\Delta t' = 39.6$ at: (c) $\Lambda^F = 70.5$, (d) $\Lambda^F = 150$, and (e) $\Lambda^F = 220$.

$0.3L$ from the upstream edge. Note the increased range of values of Λ^F over which the eigenvalues are plotted.

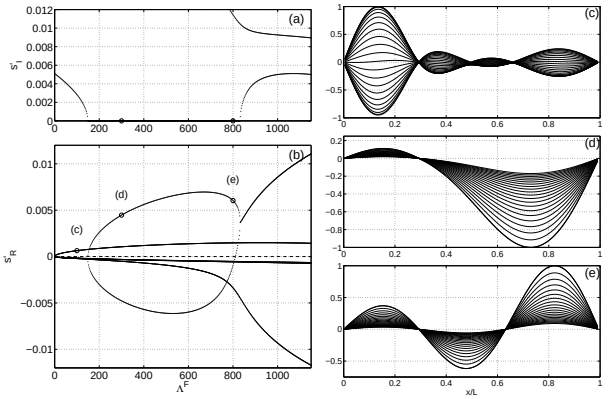

Figure 4: Elastic plate with a boundary constraint at 30% chord. Eigenvalues and snapshots of wall motion, for $t' : 0 \rightarrow 396$ over 20 time steps each of duration $\Delta t' = 19.8$ for: Mode-3 amplifying for (c) $A^F = 100$, and Mode-1 amplifying for (d) $A^F = 300$, and (e) $A^F = 800$.

For the fundamental (most unstable) mode, there now exists a pre-divergence range where wall motion is slightly attenuated. However, the third mode is unstable in this pre-divergence range. There is then a divergence loop that leads into modal coalescence-flutter type instability with no post-divergence recovery zone. The primary differences with the simple elastic plate of Fig. 2 are: a) the attenuation of most modes in the pre-divergence range; b) the increased stability of the system as a whole with the divergence onset occurring at much larger values of Λ^F; c) the lack of a post-divergence recovery zone and; d) a specific mode becomes unstable at low values of Λ^F, in the limit of $\Lambda^F \rightarrow 0$.

The increased stability of the system could be anticipated due to the fact that a hinge joint shortens the effective length of the elastic plate. Basing Λ^F on the length of the longest part of the divided wall places the divergence loop into a similar range of values as seen in Fig. 2. However, we note the appearance of a new instability that occurs in the limit of zero flow speed. Fig. 4c reveals that this principally comprises the third in-vacuo mode which is destabilised by the inclusion of the additional hinge joint. This single-mode flutter is amenable to stabilisation through the inclusion of structural damping. Results not presented here show that, for example, when $d' = 0.082$, the non-dimensional flow speed rises to $\Lambda^F = 400$ and divergence then becomes the critical instability with increasing flow speed. This new instability is discussed in detail in Section 5 below.

Figure 5 is for the same configuration as Fig. 4, except that the hinge joint has been placed at $0.5L$. The shape of the eigenvalue loci in Fig. 5 differs from Figs. 4 and 2 in that two divergence loops now exist. Figs. 5c and 5d show the corresponding eigenmode snapshots for the inner and outer divergence loops respectively at $\Lambda^F = 1000$. Two divergence loops appear because the addition of a hinge joint at 50% introduces more possible configurations for instability to occur. Divergence-type instability may occur on either half of the divided panel with each half destabilising in-phase or out-of-phase (as seen in Figs. 5c and 5d respectively). There also exists a small amount of higher-mode instability in the limit of $\Lambda^F \rightarrow 0$, although this instability is not as severe as that in Fig. 4.

5. ON THE SINGLE-MODE FLUTTER OF FLEXIBLE PANELS

We now investigate the mechanism for the pre-divergence-onset single-mode flutter seen in Figs. 4 and 5 that appeared with the introduction of an additional constraint on the flexible panel. We first note that it is the third mode that becomes unstable. Fig. 2 indicates that this mode is neutrally stable for the standard case of an elastic plate held at just its ends; we present its eigenmode at $\Lambda^F = 25$ in Fig. 6a. In Fig. 6b, we plot the phase angle of the three components

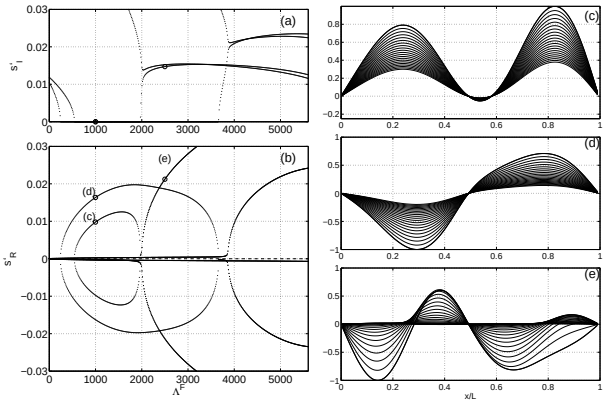

Figure 5: Elastic plate with a boundary constraint at 50% chord. Eigenvalues and snapshots of wall motion, for $t' : 0 \rightarrow 99$ over 20 time steps each of duration $\Delta t' = 4.95$ for: (c) Mode-1 amplifying for $A^F = 1000$, (d) Mode-2 amplifying for $A^F = 1000$, and (e) Mode-3 amplifying for $A^F = 2500$.

of the forcing pressure given by Eqn. 4 and their total $(-\Delta p)$ relative to that of plate velocity, $\dot{\eta}$. The spatial distribution of work done by the fluid over one cycle of oscillation, $W(x)$, is the integral of $(-\Delta p)\dot{\eta}$ over one period of oscillation and then spatial integration over the entire panel yields the total work done at the interface. Without performing such integrations, it is clear that a phase-angle difference between pressure and plate velocity of $n\pi/2$ gives $W(x) = 0$ when n is an odd integer (orthogonal), a positive value when $n/2$ is even (in-phase), and a negative value when $n/2$ is odd (anti-phase). A small departure, $\pm\psi$, from exact orthogonality also provides a mechanism for irreversible energy transfer between fluid structure. Fig. 6b indicates that the phase value of total pressure is largely orthogonal to that of the velocity (the zero of the horizontal axis). Exact orthogonality of $-\Delta p$ throughout x/L would mean that zero energy transfer occurs at every point. However, this is not the case; $\pm\psi$ is seen, especially in the regions adjacent to the nodal points of the mode shape in Fig. 6a. In fact these are not exact nodes at non-zero flow speed; animations reveal that the modal motion contains a form of constrained upstream travel through its cycle. Thus, the phase departures mean that spatially-dependent irreversible energy transfer - to and from the panel - occurs through the cycle of oscillation,. However, the exact symmetry of relative phase of pressure about $x/L = 0.5$ means that these localised energy transfers sum to zero over the entire panel and hence yield the global neutral stability of this mode. We now demonstrate how the introduction of a constraint breaks the balance of energy transfers within this sum.

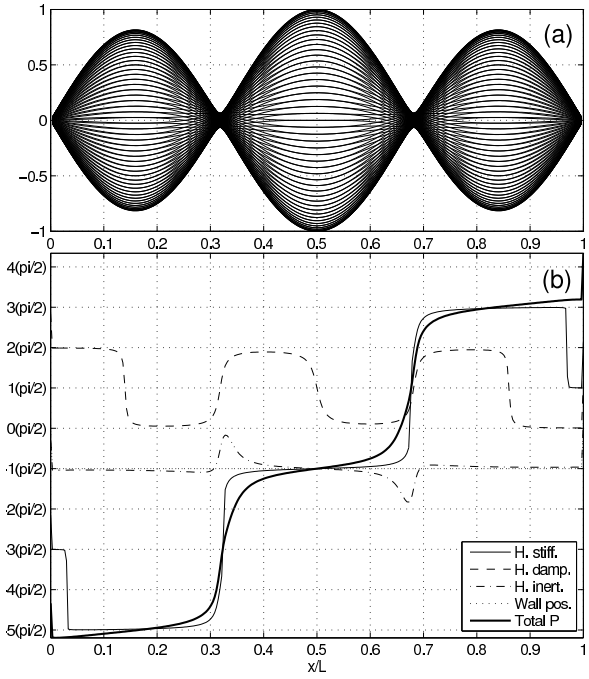

Figure 6: Standard elastic panel. Neutrally-stable third mode at $\Lambda^F = 25$, (a) snapshots of wall motion, and (b) phase of pressure loading relative to plate velocity [Legend: (1) — (thick) = total pressure; (2) — (thin) = hydrodynamic stiffness; (3) -- = hydrodynamic damping; (4) $-\cdot-$ = hydrodynamic inertia; (5) $\cdots$ = wall displacement].

A hinge constraint is introduced at the location of the upstream quasi-node seen in Fig. 6a. Eigenvalue calculations then show that this triggers third-mode flutter of the type seen in Fig. 4. Figs. 7a and 7b, at $\Lambda^F = 25$, show the mode and relative (to plate velocity) phase of pressure that can respectively be compared directly with Figs. 6a and 6b to ascertain the effect of the added constraint. We first note that the imposition of an exact upstream node forces a modification to the mode shape in its vicinity while the downstream quasi-node is largely unchanged. Contrasting the relative phase of pressure plots, a sharp change now occurs at the exact node as would be expected; however, this does confirm that it is wave-travel in the unrestrained case that creates regions of non-orthogonal pressure loading. The key feature of Fig. 7b is that the relative phase of $-\Delta p$ is not symmetric about $x/L = 0.5$ and nor are each of its constituent hydrodynamic stiffness, damping and inertia terms. The symmetry breaking occurs principally in the region

$x/L : 0.32 \rightarrow 0.5$. Over one cycle, the sum, over the whole plate, of localised irreversible energy transfers is positive and therefore the mode is globally unstable. This explanation is consistent with the stabilising effect of structural damping that provides a means of irreversible transfer *from* the plate and this offsets the net transmission of energy *to* the plate by the hydrodynamic force.

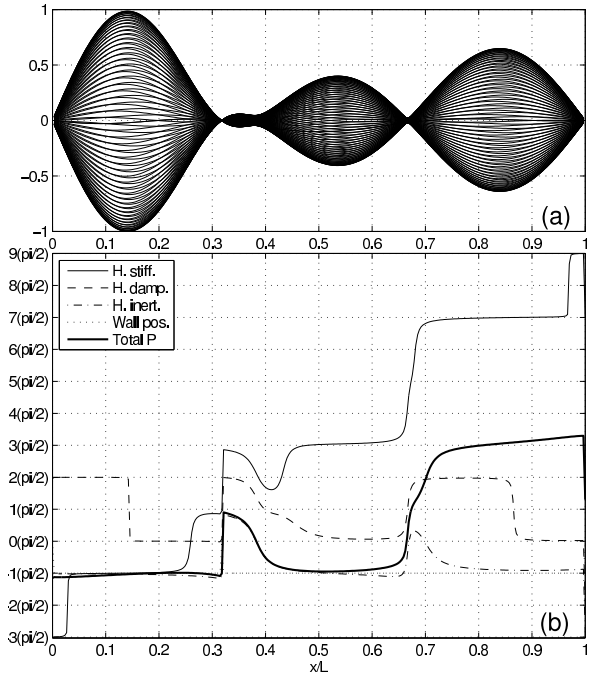

Figure 7: Elastic panel with an added hinge constraint. Single-mode flutter mode at $\Lambda^F = 25$, (a) snapshots of wall motion, and (b) phase of pressure loading relative to plate velocity [Legend as in Fig. 6b].

6. CONCLUSIONS

This paper presents the use of linear discretisation and Krylov methods for eigenvalue extraction from large matrices to give accurate determination of linearised fluid-structure interaction problems. These methods were then applied to the determination of eigenvalue loci and corresponding eigenmodes for a simple elastic plate with complex boundary conditions.

The addition of a hinge constraint within the panel's streamwise extent is found to stabilise the system with respect to divergence by decreasing the effective length of the flexible panel. However, it also makes the panel prone to flutter instability of a higher-order mode. The mechanism for this single-mode flutter is explained through an examination of the phase of the pressure loading relative to that of the plate velocity. It is shown that spatially localised irreversible energy transfers can occur. In the unrestrained case a symmetry exists for these two-way transfers that yields neutral stability for the system. Introducing a constraint breaks this symmetry and thereby triggers instability. Unlike divergence instability, this new instability can be controlled by the effect of structural damping.

7. ACKNOWLEDGEMENTS

We acknowledge the ongoing collaboration with the Fluid Dynamics Research Centre at the University of Warwick. UK. This research is supported by the Australian Research Council through the ARC-Discovery scheme.

8. REFERENCES

Dugundji, J., Dowell, E. and Perkin, B., 1963, Subsonic flutter of panels on a continuous elastic foundation. *AIAA Journal*, **1**:1146-1154.

Crighton, D.G., Oswell, J.E., 1997, Fluid loading with mean flow. I. Response of an elastic plate to localized excitation. *Philosophical Transactions of the Royal Society of London A*, **335**:557-592.

Lucey, A.D., 1998, The excitation of waves on a flexible panel in a uniform flow. *Philosophical Transactions of the Royal Society of London A*, **356(1749)**:2999-3039.

Abrahams, I.D., Wickham, G.R., 2001, On transient oscillations of plates in moving fluids. *Wave Motion*, **33**:7-23.

Pitman, M.W., Lucey, A.D., 2007, On the direct determination of the eigenmodes of finite flow-structure systems. *Proc. Roy. Soc.* (under review).

Peake, N., 2004, On the unsteady motion of a long fluid-loaded elastic plate with mean flow. *Journal of Fluid Mechanics*, **507**:335-366.

Lucey, A.D., Carpenter, P.W., 1992, A numerical simulation of the interaction of a compliant wall and an inviscid flow. *Journal of Fluid Mechanics*, **234**:121-146.

Lucey, A.D., Carpenter, P.W., Cafolla, G.J. and Yang, M., 1997, The Nonlinear Hydroelastic Behaviour of Flexible Walls. *Journal of Fluids and Structures*, **11**:717-744.